

Influence of Iron Oleate Complex Structure on Iron Oxide Nanoparticle Formation

Lyudmila M. Bronstein,^{*,†} Xinlei Huang,[†] John Retrum,[†] Abrin Schmucker,[†] Maren Pink,[†] Barry D. Stein,[‡] and Bogdan Dragnea[†]

Departments of Chemistry and Biology, Indiana University, 800 East Kirkwood Avenue, Bloomington, Indiana 47405

Received December 12, 2006. Revised Manuscript Received April 23, 2007

The dependence of iron oxide nanoparticle formation on the structure and thermal properties of Fe oleate complexes has been studied using FTIR, elemental analysis, X-ray photoelectron spectroscopy, differential scanning calorimetry (DSC), X-ray diffraction (XRD), transmission electron microscopy (TEM), and high-resolution TEM. The combination of FTIR, elemental analysis, and DSC allowed us to reveal differences between Fe oleate structures for as-synthesized and postsynthesis treated (drying and extraction with polar solvents) compounds. As-synthesized Fe oleate was found to contain a significant fraction of oleic acid, which works as a modifier altering the decomposition process and as an extra stabilizer during iron oxide nanoparticle formation. The thermal treatment of as-synthesized Fe oleate at 70 °C leads to removal of the crystal hydrate water and dissociation of oleic acid dimers, leading to a more thermally stable iron oleate complex whose final decomposition occurs at about 380 °C. Extraction of the as-prepared iron oleate complex with ethanol and acetone results in the removal of oleic acid, leading to complete reorganization of the Fe oleate complex and a dramatic change of its thermal behavior. It mainly leads to an increase in the iron oxide nucleation temperature, thus decreasing the kinetic separation between nucleation and growth processes and affecting the particle size and particle size distribution. When the separation between these processes was about 5 °C, polydisperse nanoparticles were formed, whereas larger temperature separation values allow the formation of monodisperse nanoparticles with sizes in the 8.5–23.4 nm range. The XRD data indicate that iron oxide nanoparticles contain two phases: wüstite and spinel, with the spinel fraction depending on the conditions of the nanoparticle formation.

1. Introduction

Magnetic nanoparticles (NPs) have gained considerable attention in the past decade driven by their broad technological applications including single-bit elements in high-density magnetic data storage arrays,^{1,2} ferrofluids,^{3,4} contrast enhancement agents for magnetic resonance imaging,^{5,6} bioprobes,⁷ cell sorters,^{8,9} etc. Iron oxide NPs are often favored for biomedical applications because they are generally stable under air and can be metabolized or degraded in vivo.^{10,11} One of the popular methods for synthesizing monodisperse iron oxide NPs is high-temperature decom-

position of iron compounds with oxygen-containing ligands such as acetylacetonates,^{1,12,13} acetates,¹³ or oleates^{14,15} in surfactant-containing solutions. The narrow particle size distribution is due to the separation on the temperature scale of nucleation and growth processes.^{14,15} Depending on the reaction conditions, different shapes, sizes, and crystal structures of iron oxide nanoparticles can be obtained. Iron acetylacetonate can also be decomposed in a vapor phase, forming iron oxide nanorods.¹⁶

The advantage of the procedures based on Fe oleate decomposition is that iron oxide NPs can be prepared in a wide range of sizes (from 6 to 30 nm)^{14,15} merely by varying the reactions conditions. It is noteworthy that in this method even large particles are obtained in one step without a seeding procedure.¹ Such a variety of sizes of monodisperse magnetic nanoparticles is especially important, as it serves the stringent special scale demands of the specific applications discussed

* To whom correspondence should be addressed. E-mail: lybronst@indiana.edu.

† Department of Chemistry, Indiana University.

‡ Department of Biology, Indiana University.

- (1) Sun, S.; Zeng, H. *J. Am. Chem. Soc.* **2002**, *124*, 8204.
- (2) Frolov, G. I. *Tech. Phys.* **2001**, *46*, 1537.
- (3) Sestier, C.; Da-Silva, M. F.; Sabolovic, D.; Roger, J.; Pons, J. N. *Electrophoresis* **1998**, *19*, 1220.
- (4) Racuciu, M.; Creanga, D. E.; Calugaru, G. *J. Optoelectron. Adv. Mater.* **2005**, *7*, 2859.
- (5) Bulte, J. W.; Kraitchman, D. L. *NMR Biomed.* **2004**, *17*, 484.
- (6) Mulder, W. J. M.; Strijkers, G. J.; van Tilborg, G. A. F.; Griffioen, A. W.; Nicolay, K. *NMR Biomed.* **2006**, *19*, 142.
- (7) Chemla, Y. R.; Crossman, H. L.; Poon, Y.; McDermott, R.; R.; S.; Alper, M. D.; Clarke, J. *Proc. Natl. Acad. Sci.* **2000**, *97*, 14268.
- (8) Pamme, N.; Wilhelm, C. *Lab Chip* **2006**, *6*, 974.
- (9) Chatterjee, J.; Haik, Y.; Chen, C. J. *J. Magn. Magn. Mater.* **2001**, *225*, 21.
- (10) Hellstern, D.; Schulze, K.; Schopf, B.; Petri-Fink, A.; Steitz, B.; Kamau, S.; Hilbe, M.; Koch-Schneidemann, S.; Vaughan, L.; Hottiger, M.; Hofmann, M.; Hofmann, H.; von Rechenberg, B. *J. Nanosci. Nanotechnol.* **2006**, *6*, 3261.

- (11) Briley-Saebø, K.; Bjørnerud, A.; Grant, D.; Ahlstrom, H.; Berg, T.; Kindberg, G. M. *Cell Tissue Res.* **2004**, *316*, 315.
- (12) Li, Z.; Chen, H.; Bao, H.; Gao, M. *Chem. Mater.* **2004**, *16*, 1391.
- (13) Redl, F. X.; Black, C. T.; Papaefthymiou, G. C.; Sandstrom, R. L.; Yin, M.; Zeng, H.; Murray, C. B.; O'Brien, S. P. *J. Am. Chem. Soc.* **2004**, *126*, 14583.
- (14) Yu, W. W.; Falkner, J. C.; Yavuz, C. T.; Colvin, V. L. *Chem. Commun.* **2004**, 2306.
- (15) Park, J.; An, K.; Hwang, Y.; Park, J.-G.; Noh, H.-J.; Kim, J.-Y.; Park, J.-H.; Hwang, N.-M.; Hyeon, T. *Nat. Mater.* **2004**, *3*, 891.
- (16) Wu, J.-J.; Lee, Y.-L.; Chiang, H.-H.; Wong, D. K.-P. *J. Phys. Chem. B* **2006**, *110*, 18108.

above. Because we are interested in such applications as virus studies,^{17–19} magnetic “stoppers” in separation membranes,²⁰ near-field nanoparticle transducers,²¹ etc. comparatively large magnetic NPs are needed. For example, when magnetic NPs are used for templating the Brome mosaic virus (BMV) capsids, the large particles allow one to avoid virus capsid distortion or incorporation of several particles in a single virus capsid.¹⁹ These large particles can be obtained in one step via the iron oleate route.

Iron oleate used for NP synthesis can be synthesized either by dissolution of various iron oxides or hydroxides in oleic acid¹⁴ or by reaction between iron(III) chloride and sodium oleate.¹⁵ In both cases, the influence of reaction conditions such as a reaction temperature (i.e., solvent bp), time, and Fe/oleic acid molar ratio were varied, but in neither method was the structure of iron oleate complexes and its influence on the nanoparticle formation interrogated. Using FTIR, elemental analysis, and differential scanning calorimetry (DSC), we discovered that the iron oleate complex structure determines the conditions of thermal decomposition of the iron oleate complex, i.e., nucleation and growth conditions, and therefore the NP formation.

In this paper, we report for the first time the structure of iron oleate complexes prepared by interaction of Fe(III) chloride and sodium oleate and the influence of postsynthesis treatment on the iron oleate complex structure and the NP formation, offering an additional key insight on the mechanism of the NP synthesis via the Fe oleate route. We demonstrate that the temperature separation between nucleation and growth processes obtained from DSC combined with the choice of the thermolysis processing temperature can be used as a quality test in anticipating the resultant particle size distribution.

2. Experimental Section

2.1. Materials. FeCl₃·6H₂O (98%), docosane (99%), eicosane (99%), and octadecane (99%) were purchased from Sigma-Aldrich and used as received. Hexanes (85%), ethanol (95%), and acetone (99.78%) were purchased from EMD and used as received. Chloroform (Mallinckrodt, 100%), oleic acid (TCI, 95%), and oleic acid sodium salt (ScienceLab.com, 95%) were used without purification.

2.2. Syntheses. **2.2.1. Synthesis of Fe Oleate Complex.** The synthesis of iron oleate was carried out using a published procedure.¹⁵ In a typical experiment, 3.24 g of FeCl₃·6H₂O (12 mmol) was dissolved in 12 mL of distilled water, filtered, and mixed with 10.95 g of sodium oleate (40 mmol), 24 mL of ethanol, 6 mL of distilled water, and 42 mL of hexane. The solution was heated to 70 °C and stirred at this temperature for 4 h under an argon

Table 1. Elemental Analysis Data of Fe Oleate Complexes

sample notation	elemental analysis data (%)		
	C	H	Fe
Fe oleate dried at 30 °C (FeOI-1)	70.47	11.04	6.17
Fe oleate dried at 70 °C (FeOI-2)	71.90	10.61	6.07
Fe oleate after extraction and drying at 30 °C (FeOI-3)	61.21	9.67	13.00
Fe oleate after extraction and drying at 70 °C (FeOI-4)	60.42	9.84	14.2
(C ₁₈ H ₃₆ COO) ₂ (C ₁₈ H ₃₆ COOH)FeO _{1/2} ·H ₂ O	70.44	11.43	5.77
(C ₁₈ H ₃₆ COO) ₂ (C ₁₈ H ₃₆ COOH)FeO _{1/2}	71.77	11.44	5.88
(C ₁₈ H ₃₆ COO) ₂ Fe ₂ O ₂ ·3C ₂ H ₅ OH	60.41	10.30	12.81
(C ₁₈ H ₃₆ COO) ₂ Fe ₂ O ₂ ·2C ₂ H ₅ OH	59.85	10.22	13.96

flow. When the reaction was complete, the upper red-brownish organic layer containing the iron oleate complex was separated and washed three times with 9 mL of distilled water in a separatory funnel. Next, hexane was evaporated using a rotary evaporator. The resultant iron oleate complex was dried in a vacuum oven at 30 or 70 °C for 24 h. The final product is a reddish-brown viscous oil. In the case of the free oleic acid removal (see Results and Discussion), the product was washed twice with ethanol and twice with acetone before drying. After extraction and drying (30 or 70 °C in a vacuum oven for 24 h), the product is a waxy solid. The elemental analysis data are presented in Table 1.

2.2.2. Synthesis of Iron Oxide Nanoparticles. The synthesis of iron oxide nanoparticles was carried out by modification of a procedure published elsewhere.¹⁵ In a typical experiment for 20.1 nm NPs, 2.78 g (3 mmol) of iron oleate complex (thermally treated at 70 °C in a vacuum oven for 24 h), 0.96 mL of oleic acid (3 mmol), and 10 mL of docosane (hydrocarbon C₂₂H₄₆, solid at room temperature) were combined in the three-neck round-bottom reaction flask. The mixture was first heated to 60 °C to melt the solvent, which allowed the reactants to dissolve under vigorous stirring. The reaction mixture was then heated to about 370 °C with a heating rate of 3.3 °C/min under stirring (using a temperature controller and set temperature of 380 °C) and was kept refluxing for 3 min. The initial reddish-brown color of the reaction solution turned brownish-black. The resultant solution was then cooled down to 50 °C and a mixture of 10 mL of hexane and 40 mL of acetone was added to the reaction flask to precipitate the NPs. The NPs were separated by centrifugation and washed 3 times by a mixture of hexane and acetone. After washing, the resultant NPs were separated by centrifugation and dissolved in chloroform for long-term storage. Alternatively, only a small fraction of the reaction solution was precipitated as described above, whereas the major fraction was kept as a solid solution and precipitated when needed. The latter procedure avoids NP aggregation in a liquid solution during prolonged storage time.

The data on variation of the reaction conditions are presented in Table 2.

2.3. Characterization. Fourier transform infrared (FTIR) spectra were recorded on a Nicolet spectrometer. The samples were prepared by evaporating the chloroform solutions of iron oleate complexes on the KBr disk.

Elemental analysis on Fe was carried out using X-ray fluorescence measurements performed with a Zeiss Jena VRA-30 spectrometer equipped with a Mo anode, a LiF crystal analyzer, and a SZ detector. Analyses were made on the basis of the Fe K_α line, and a series of standards were prepared by mixing 1 g of polystyrene with 10–20 mg of standard compounds. The time of data acquisition was held constant at 10 s.

X-ray diffraction (XRD) patterns were collected on a Scintag θ–θ powder diffractometer with a Cu K_α source (1.54 Å).

Differential scanning calorimetry (DSC) was performed using a Q10 TA calorimeter. Indium was used to calibrate transitions.

- (17) Chen, C.; Kwak, E.-S.; Stein, B.; Kao, C. C.; Dragnea, B. *J. Nanosci. Nanotechnol.* **2005**, *5*, 2029.
- (18) Chen, C.; Daniel, M.-C.; Quinkert, Z. T.; De, M.; Stein, B.; Bowman, V. D.; Chipman, P. R.; Rotello, V. M.; Kao, C. C.; Dragnea, B. *Nano Lett.* **2006**, *6*, 611.
- (19) Dixit, S. K.; Goicochea, N. L.; Daniel, M.-C.; Murali, A.; Bronstein, L.; De, M.; Stein, B.; Rotello, V. M.; Kao, C. C.; Dragnea, B. *Nano Lett.* **2006**, *6*, 1993.
- (20) Guliants, V. V.; Carreon, M. A.; Lin, Y. S. *J. Membr. Sci.* **2004**, *235*, 53.
- (21) Kwak, E.-S.; Onuta, T.-D.; Amarie, D.; Potyraiolo, R.; Stein, B.; Jacobson, S. C.; Schaich, W. L.; Dragnea, B. *J. Phys. Chem. B* **2004**, *108*, 13607.

Table 2. Conditions of the Syntheses of Iron Oxide Nanoparticles and Their Characteristics

solvent (bp (°C))	Fe oleate complex	Fe oleate conc. (mg/mL)	oleic acid conc. (mL/mL)	refluxing time (min)	NP size (nm)	NP shape
docosane (375)	FeOl-2	0.2	0.064	3	23.4	spherical
docosane (375)	FeOl-2	0.3	0.096	3	20.1	spherical
eicosane (357)	FeOl-2	0.2	0.064	30	17.9	spherical
octadecane (318)	FeOl-1	0.2	0.096	60	10.6	spherical
octadecane (318)	FeOl-1	0.2	0.096	30	8.5	spherical
eicosane (357)	FeOl-1	0.3	0.096	30	18.6	cubic
docosane (375)	FeOl-4	0.2	0.224	3	19.5	spherical
docosane (375)	FeOl-3	0.2	0.224	3	14–28 for spheres	spherical, fused, rods

Samples weighing between 7 and 18 mg were sealed in aluminum pans and heated once from 40 to 400 °C at a rate of 10 °C/min in nitrogen flow.

Electron-transparent specimens for transmission electron microscopy (TEM) were prepared by placing a drop of dilute solution onto a carbon-coated Cu grid. Images were acquired at an accelerating voltage of 80 kV on a JEOL JEM1010 scanning transmission electron microscope. High-resolution TEM (HRTEM) images were acquired at an accelerating voltage of 200 kV on a JEOL 2200FS transmission electron microscope.

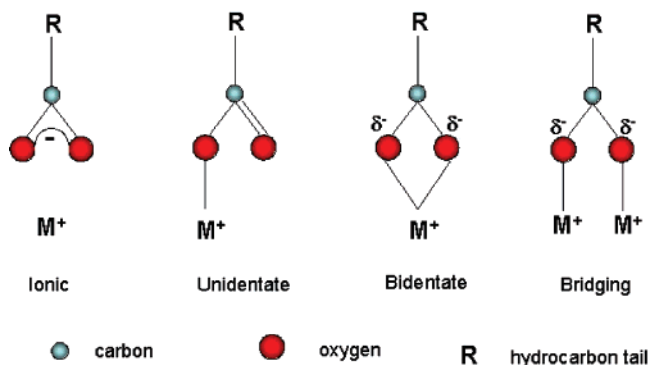
X-ray photoelectron spectra (XPS) were obtained using Mg K α ($h\nu = 1253.6$ eV) monochromatized radiation with a modified ES-2403 spectrometer (provided by the Institute for Analytic Instrumentation of the Russian Academy of Sciences, St. Petersburg, Russia). The analyzer was operated at a pass electron energy of 100 eV. All data were acquired at an X-ray power of 100 W and an energy step of 0.1 eV. The electron-flood gun accessory was used so that the current of the total emitted electron flux from the flood-gun filament was adjustable from 0 to 100 mA, with the optimum found to be 70 mA at an electron energy of 2 eV. Samples were allowed to outgas for 15–30 min before analysis and were sufficiently stable during examination. Data analysis was performed using a standard RFES-set with Resolver program.

3. Results and Discussion

To form iron oxide nanoparticles in the 8–23 nm diameter range, we modified the published procedure¹⁵ using thermal decomposition of iron oleate complex in the presence of oleic acid as a surfactant. As was established previously,¹⁵ the variation of reaction temperature allows us control over the particle size. We used saturated hydrocarbons of different length as a solvent because (a) they enable a variety of the boiling temperatures, (b) they are more chemically inert at high temperatures than many other solvents, and (c) they are solid at room temperature. The last factor allows storage of NPs in solid solutions without aggregation and loss of particle solubility. We discovered that a secondary treatment of iron oleate complexes synthesized by interaction of equimolar amounts of ferric chloride and sodium oleate¹⁵ strongly influences the particle formation. This prompted us to study the iron oleate complex structure.

3.1. Fe Oleate Structure. As-synthesized iron oleate prepared by the literature procedure¹⁵ is a dark-brown, viscous liquid. The structure of Fe oleate was studied using FTIR, elemental analysis, DSC, and XPS. Four different types of coordination modes can be envisioned for metal carboxylates (Scheme 1): ionic, unidentate, bidentate, and bridging.²²

Scheme 1. Types of Metal Carboxylate Coordination Modes; For Simplicity, the Monovalent Metal Is Shown Instead of Trivalent



3.1.1. FTIR. The characteristic IR bands for metal carboxylates are in the range of 1650–1510 cm^{-1} for the asymmetrical vibrations and 1400–1280 cm^{-1} for the symmetrical vibrations.²² Figure 1 presents the FTIR spectra of oleic acid and two Fe oleates prepared according to the published procedure¹⁵ and dried in vacuum at the two different temperatures: 30 (FeOl-1) and 70 °C (FeOl-2). The FTIR spectra of both Fe oleates contain several strong bands in the $\nu(\text{COO}^-)$ region: 1711, 1607, 1519, and 1444 cm^{-1} . The band at 1711 cm^{-1} can be assigned either to the carbonyl group of oleic acid (Figure 1)^{23,24} or to asymmetric vibrations of unidentate carboxylate,²² although the latter is less common. Park et al.¹⁵ assigned the band at 1608 cm^{-1} to C=C group. However, we believe this assignment is incorrect because neither oleic acid (Figure 1) nor Na oleate exhibit this band in the FTIR spectra. In general, in nonconjugated compounds, the C=C stretching vibration gives rise to a weak IR band in the range 1660–1640 cm^{-1} , and very often, it cannot be seen because of overlapping with strong carbonyl vibrations or because of the trans-symmetry of the double bond.^{25,26} We therefore assume that vibrational frequencies at 1608, 1519, and 1444 cm^{-1} belong to carboxylate groups.

The position and separation of $\nu(\text{COO}^-)$ bands, Δ , in the 1300–1700 cm^{-1} region can be used to deduce the carboxylate coordination mode.^{22–24,27} For $\Delta > 200$ cm^{-1} , a unidentate ligand is expected,²⁷ whereas for $\Delta < 110$ cm^{-1} , it is a bidentate ligand. For a bridging ligand, Δ is between

(23) Abrahamson, H. B.; Lukaski, H. C. *J. Inorg. Biochem.* **1994**, *54*, 115.

(24) Soederlind, F.; Pedersen, H.; Petoral, R. M.; Kaell, P.-O.; Uvdal, K. *J. Colloid Interface Sci.* **2005**, *288*, 140.

(25) Bellamy, L. J. *The Infrared Spectra of Complex Molecules*, 3rd ed.; Chapman and Hall: London, 1975; p 433.

(26) Sinclair, R. G.; McKay, A. F.; Myers, G. S.; Jones, R. N. *J. Am. Chem. Soc.* **1952**, *74*, 2578.

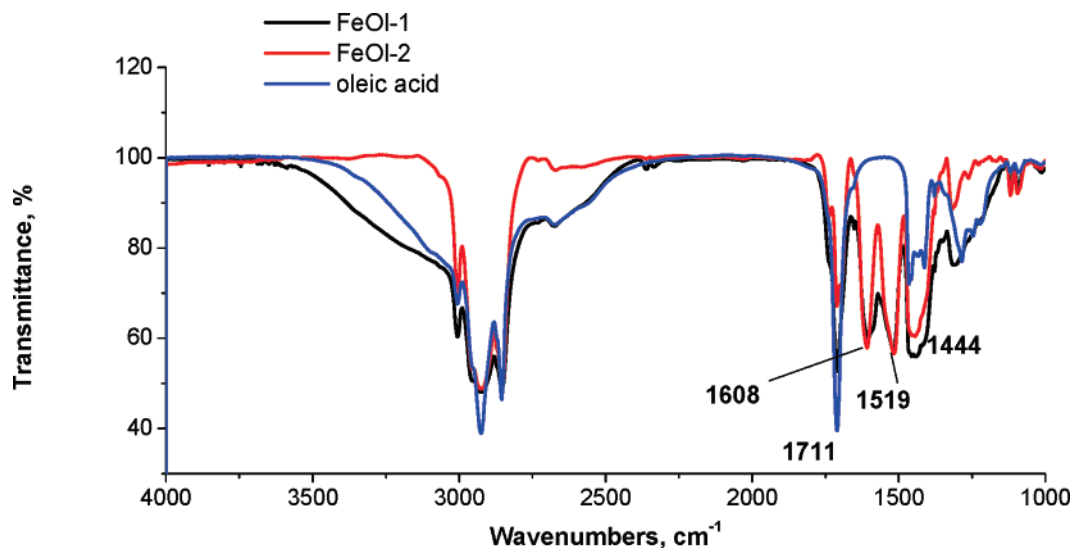


Figure 1. FTIR spectra of oleic acid and Fe oleates dried at 30 (FeOI-1) and 70 °C (FeOI-2).

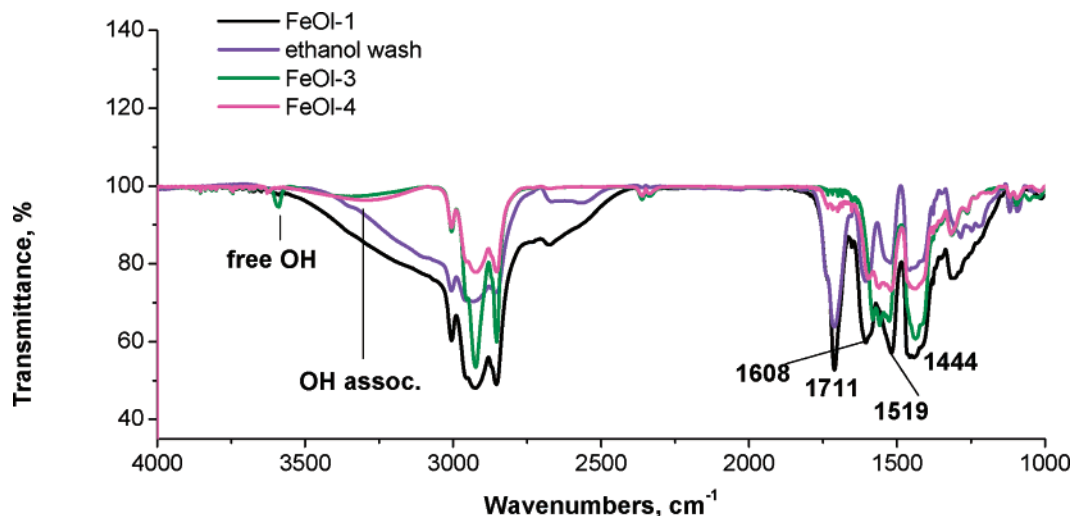


Figure 2. FTIR spectra of FeOI-1, Fe oleates after extraction with ethanol and acetone and drying at 30 (FeOI-3) and 70 °C (FeOI-4), and the ethanol wash.

140 and 200 cm^{-1} . For Fe oleate, the difference between two characteristic bands at 1519 and 1444 cm^{-1} is 75 cm^{-1} , revealing bidentate coordination. Because the 1444 cm^{-1} band may result from overlap of the $\nu(\text{COO}^-)$ stretching and $\delta(\text{CH}_2)$ scissoring bands, its position can be uncertain. The shoulder on the peak at 1443 cm^{-1} is at about 1415 cm^{-1} , making $\Delta = 104$ and still matching the bidentate coordination. We believe that the peak at 1608 cm^{-1} is a result of band splitting (a doublet at 1608 and 1519 cm^{-1}) due to the presence of two coordination modes: bidentate and bridging (or unidentate²⁷) coordination (Δ is either 193 or 165 cm^{-1}).²⁴ The very broad shoulder at about 3300 cm^{-1} in the FTIR spectra of oleic acid and FeOI-1 is assigned to the dimers of oleic acid. The absence of this band in the FeOI-2 spectrum reveals dissociation of the oleic acid dimers upon heating at 70 °C.

When as-prepared iron oleate is washed twice with ethanol and acetone and dried at 30 °C (FeOI-3), the FTIR spectrum of the solid changes dramatically (Figure 2). It contains

vibrations at 1527 and 1436 cm^{-1} , but no bands at 1711 and 1608 cm^{-1} , whereas the FTIR spectrum of the ethanol wash contains a strong band at 1711 cm^{-1} . As was indicated for ferric stearate, ethanol extraction easily removes stearic acid.²³ We believe that in our case, when oleic acid is removed by extraction (oleic acid is formed because of hydrolysis of sodium oleate during the reaction), the Fe oleate is more regularly packed and only bidentate coordination ($\Delta = 91 \text{ cm}^{-1}$) of the oleate ligand is observed. This is consistent with observations for Ca carboxylates²² when the splitting of the asymmetric carboxylate group stretching vibrations was observed only for disordered phases with three-dimensional complexes. The oleic acid impurity removed with ethanol (see the ethanol wash in Figure 2) provides an additional degree of freedom in Fe oleate coordination. The FTIR spectrum of the acetone wash does not differ from that of washed Fe oleate, but after being washed with acetone, Fe oleate becomes a waxy solid, revealing that some unidentified impurity is removed with the acetone extraction. The sharp band at 3589 cm^{-1} in the FTIR spectrum of FeOI-3 is due to the free OH group of ethanol, whereas the broad band at about 3270 cm^{-1} is characteristic of the OH group association (coordination).²⁵

(27) Nakamoto, K. *Infrared and Raman Spectra of Inorganic and Coordination Compounds, Part B: Applications in Coordination, Organometallic and Bioinorganic Chemistry*, 5th ed.; Wiley: New York, 1997; p 387.

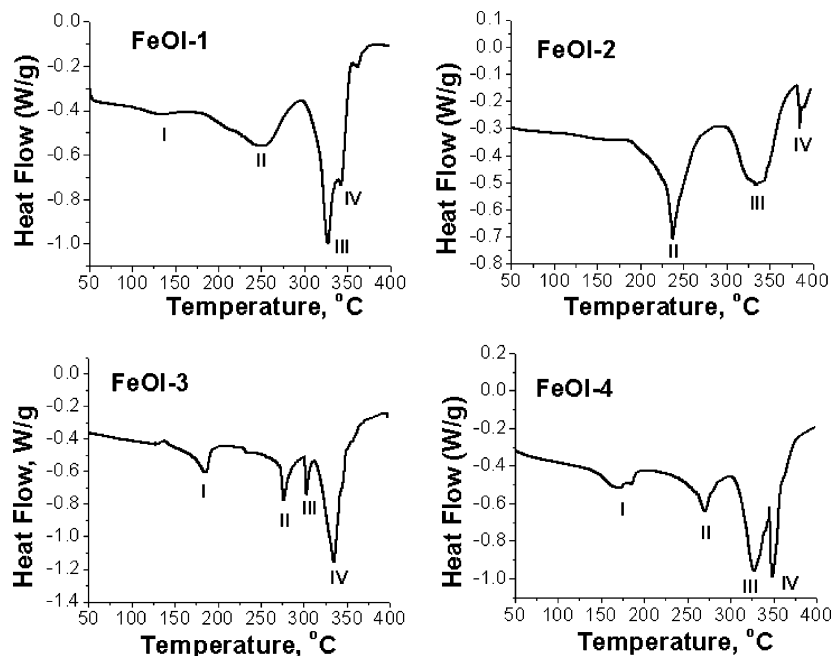
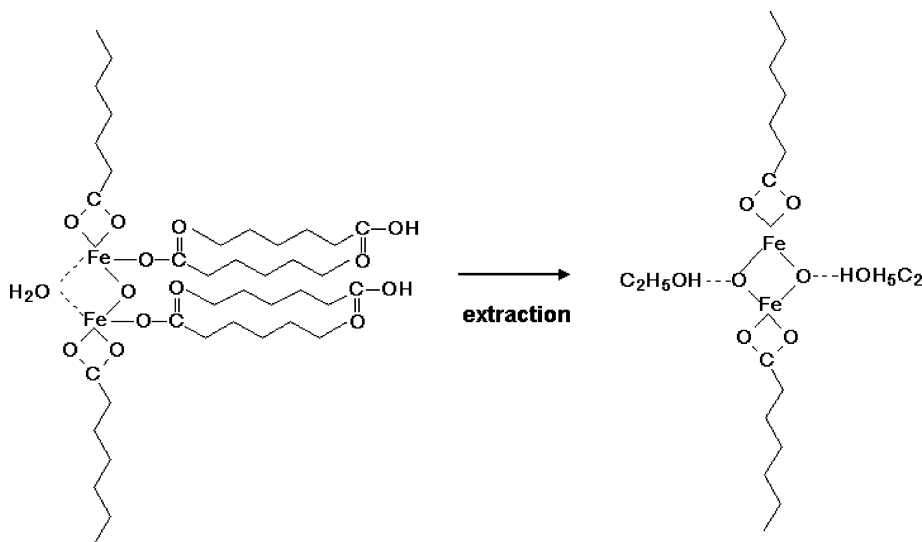


Figure 3. DCS traces of FeOI-1, FeOI-2, FeOI-3, and FeOI-4. The labeled transitions correspond to (I) removal of water or ethanol, (II) nucleation, (III) growth, (IV) and final precursor decomposition.

Scheme 2. Structure of Iron Oleate Complexes before (FeOI-1, left) and after (FeOI-4, right) Extraction with Ethanol



The presence of these bands confirms inclusion of ethanol in the Fe oleate complex structure. The incorporation of alcohol molecules into the Fe carboxylate structure was reported earlier.²⁸ The drying of FeOI-3 at 70 °C leads to removal of only nonassociated ethanol (Figure 3), whereas coordinated ethanol molecules remain in the sample.

3.1.2. Elemental analysis and XPS. The elemental analysis data for the Fe oleate complexes discussed above are presented in Table 1.

The elemental analysis data show that Fe oleate dried at 30 °C (FeOI-1) most likely contains three oleates, one crystal hydrate water molecule, and half an oxygen per each Fe. Because the FTIR data prove the presence of oleic acid, we think that the most probable structure is a dimer (Scheme 2, left) containing a bidentate and unidentate ligand per Fe ion,

whereas oleic acid is attached to Fe oleate either because of hydrophobic interactions (shown) or hydrogen bonding (as a water molecule). The presence of crystal hydrate water cannot be confirmed by FTIR because of very broad OH band associated with the oleic acid dimer (see above). According to elemental analysis data, after being dried at 70 °C, the crystal hydrate water is mainly removed (Table 1), which is corroborated by the absence of the relevant bands around 3300 cm^{-1} in the FTIR spectrum of FeOI-2. In addition, dissociation of oleic acid dimers took place (see the FTIR section). Extraction with ethanol and acetone allows for removal of oleic acid followed by a structural change: both oleate ligands become bidentate, as shown in Scheme 2 (right). Both elemental analysis and FTIR are consistent with the inclusion of ethanol molecules in the Fe oleate complex structure, yet in FeOI-3 (drying at 30 °C), about three ethanol molecules are included, both associated (co-

ordinated) and free (Figure 3), whereas FeOI-4 contains only two coordinated ethanol molecules (Table 1, Figure 2).

XPS data demonstrate that all four Fe oleate samples contain C, O, and Fe, and also Si impurities; the last might come from the glassware. No Cl or Na is found. The deconvolution of the high-resolution XPS Fe 2p spectra (see the Supporting Information, Figure S1 for FeOI-3) demonstrates that in Fe oleate complexes, only the Fe(III) (Fe 2p_{3/2} peak in the range 711.5–711.8 eV) species are present, revealing the absence of Fe(III) reduction, which would form mixed-valence trinuclear iron oleate complexes, [Fe₃O(O₂-CR)₆L₃], reported elsewhere.^{29,30} Below, we demonstrate that the structural difference of the Fe oleates influences their decomposition behavior and hence the nanoparticle formation.

3.1.3. DSC. The DSC traces of Fe oleate complexes treated in the above conditions are presented in Figure 3. The DSC trace of FeOI-1 shows a small endothermic peak at 132 °C that can be assigned to the removal of crystal hydrate water because the DSC trace of FeOI-2 dried at 70 °C shows no transitions in this temperature range. This corroborates the FTIR and elemental analysis data. According to ref 15, upon decomposition of the Fe oleate complex, one oleate group dissociates from the precursor at 200–240 °C, whereas the two remaining oleate ligands dissociate at about 300 °C. On the basis of our analysis of the FTIR, elemental analysis, and DSC data of the Fe oleate complexes dried at different temperatures but not subjected to the extraction, the second endothermic transition with an onset at about 183–189 °C may be related to the removal of free oleic acid or partially unidentate oleate ligand. This transition has been assigned to the formation of nuclei.¹⁵ The third transition, with an onset at about 300 °C for both samples, should lead to the removal of the remaining oleate ligands and formation of iron oxide nanoparticles. However, FeOI-2 shows a much broader third transition than FeOI-1 and an additional endothermic peak with an onset at 380 °C, revealing that the complete decomposition (or restructurization) of the Fe oleate precursor occurs only at about 380 °C. Another important difference between FeOI-1 and FeOI-2 is that for the former, the second and third transitions (nucleation and particle growth, respectively) are separated by only about 10 °C, whereas for the latter, this separation is about 20 °C. Because separation of nucleation and growth processes in time and/or on the temperature scale is crucial for synthesis of monodisperse nanoparticles,³¹ one might expect that, in similar conditions, FeOI-1 should yield more polydisperse particles than FeOI-2.

When oleic acid is removed from the Fe oleate complex by extraction and the sample is dried at 30 °C (FeOI-3), the DSC trace shows a pronounced endothermic transition with an onset at 138 °C ($\Delta H = 24$ J/g), which we assign to the removal of ethanol molecules (Scheme 2, right). Here, the

second endothermic transition onsets at the higher temperature than for non-extracted samples (~230 vs 183–189 °C), indicating different conditions and probably a different mechanism for the nucleus formation. The very sharp (but weak) transition onsets at 300 °C (similar to the nonextracted sample), whereas the final decomposition starts at 312 °C, yielding a separation between the second and third transitions of only 5 °C. No endothermic peak at about 380 °C is observed.

The DSC trace of FeOI-4 (extracted and dried at 70 °C) differs from that of FeOI-3 by a decreased intensity of the first endothermic transition associated with the removal of ethanol molecules ($\Delta H = 17$ J/g), corroborating the FTIR and elemental analysis data on partial removal of ethanol under drying in a vacuum at 70 °C. The second transitions for FeOI-3 and FeOI-4 are similar (with $\Delta H = 26$ J/g), whereas the final decomposition processes differ significantly. For FeOI-4, this results in a separation between the second and third transitions of 13 °C. The partial removal of ethanol under drying at 70 °C evidently affects the decomposition process. Very small separation between nucleation and growth processes for FeOI-3 should make the formation of monodisperse nanoparticles difficult. In the next section, we demonstrate the influence of the thermal properties of differently treated Fe oleate complexes along with reaction conditions on nanoparticle formation.

3.2. Fe Oxide Nanoparticle Formation. 3.2.1. TEM.

Using Fe oleate complexes FeOI-1 and FeOI-2 and varying the reaction temperature, concentration, and the reaction time (Table 2), we prepared spherical monodisperse particles of 23.4, 20.1, 17.9, 10.6, and 8.5 nm diameter (Figure 4). The histograms of the TEM images presented in Figure 4 show that in all the cases, the particle size distributions are narrow (the standard deviation is below 10%) so the particles are practically monodisperse (Figure 5).

When FeOI-1 was used as a precursor, in octadecane, it resulted in small monodisperse spherical particles the size of which depend on the reaction time (Table 2, panels d and e in Figure 4), whereas in eicosane, it leads to well-defined monodisperse cubic particles (Figure 4f). At the same time, in docosane, the particles derived from FeOI-1 are very polydisperse (see the Supporting Information, Figure S2). We believe that in this case, because of a relatively small separation between the endothermic transitions, which are responsible for nucleation and growth (~10 °C), the increase in the reaction temperature to the solvent boiling point (375 °C) even with the slow heating rate (of 3.3 °C/min as suggested by Park et al.¹⁵) causes partial overlapping of the nucleation and growth processes, leading to a broader particle size distribution. Indeed, in the DSC trace of FeOI-1 (see the Supporting Information, Figure S3) recorded at the heating rate of 3.3 °C/min, the separation between endothermic transitions II and III is only 12 °C.

In docosane and eicosane, the monodisperse spherical particles were obtained with FeOI-2 as a precursor, whereas the lower reaction temperature (octadecane as a solvent) led to incomplete decomposition of the precursor because of the higher thermal stability of FeOI-2 compared to that of FeOI-1 (see the endothermic transition at 380 °C for FeOI-2, Figure

(29) Nakamoto, T.; Hanaya, M.; Katada, M.; Endo, K.; Kitagawa, S.; Sano, H. *Inorg. Chem.* **1997**, *36*, 4347.

(30) Nakamoto, T.; Katada, M.; Sano, H. *Inorg. Chim. Acta* **1999**, *291*, 127.

(31) Talapin, D. V.; Shevchenko, E. V.; Weller, H. Synthesis and Characterization of Magnetic Nanoparticles. In *Nanoparticles*; Schmid, G., Ed.; Wiley-VCH: Weinheim, Germany, 2004; pp 199.

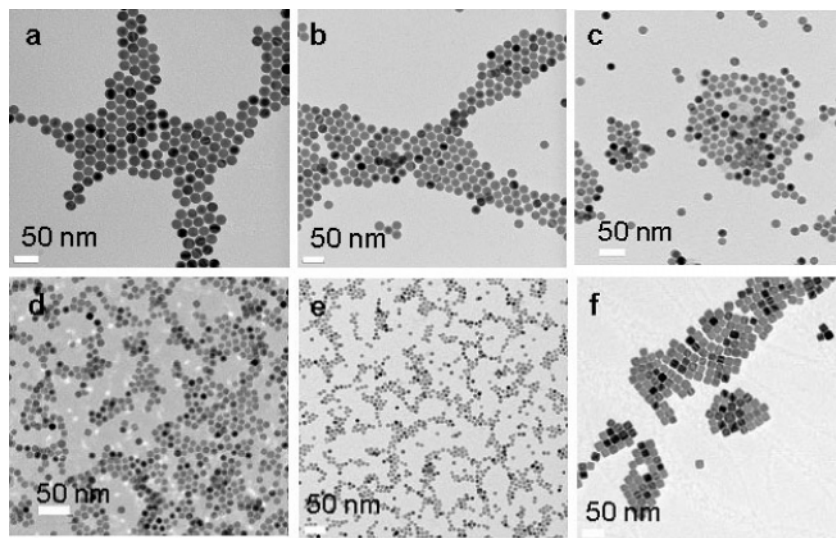


Figure 4. TEM images of (a) 23.4, (b) 20.1, (c) 17.9, (d) 10.6, and (e) 8.5 nm spheres and (f) 18.6 nm cubes.

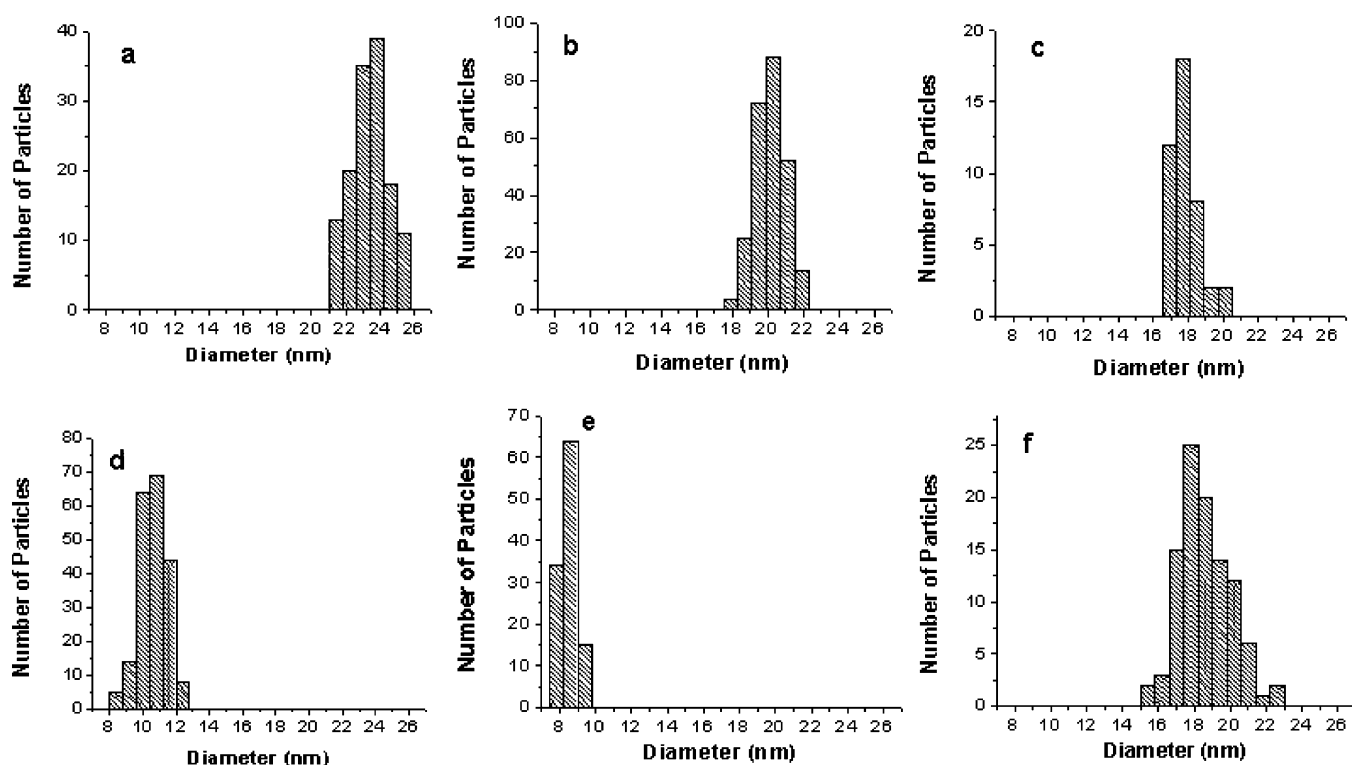


Figure 5. Histograms of the TEM images presented in Figure 4. The mean diameters and standard deviations are: (a) 23.4 nm \pm 4.4%, (b) 20.1 nm \pm 4.1%, (c) 17.9 nm \pm 4.5%, (d) 10.6 nm \pm 7.7%, (e) 8.5 nm \pm 5.2%, and (f) 18.6 nm \pm 7.7%. See Figure 4 caption for details.

3). Thus, the thermal characteristics of iron oleate dictate the choice of the temperature (kind of a solvent) to produce monodisperse nanoparticles. On the other hand, the size of the nanoparticles is clearly determined by the reaction time, temperature, and concentration.

The nanoparticle formation with the FeOI-4 proceeds dramatically differently. To provide proper nanoparticle stabilization and prevent particle aggregation, we should increase the amount of oleic acid (surfactant) by a factor of 3.5, reflecting on the role of oleic acid impurity in FeOI-1 and FeOI-2 serving as a stabilizer of the nanoparticles formed. In addition, in the same conditions (Table 2), instead of 23.4 nm NPs, fairly monodisperse 19.5 nm \pm 2.4% (Figure 6a) NPs are formed. At the same time, the crystalline

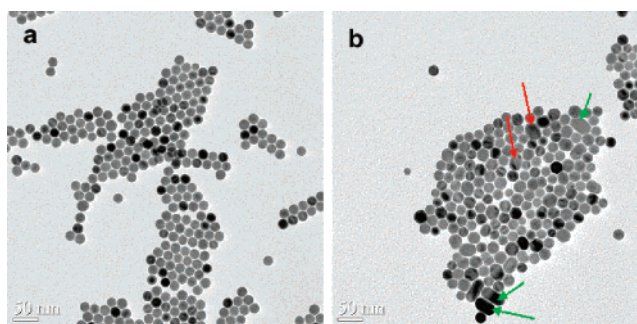


Figure 6. TEM image of (a) 19.5 nm monodisperse nanoparticles prepared from FeOI-4 and (b) polydisperse nanoparticles derived from FeOI-3.

structures of these particles are very similar (see the XRD pattern in the Supporting Information, Figure S4). As we

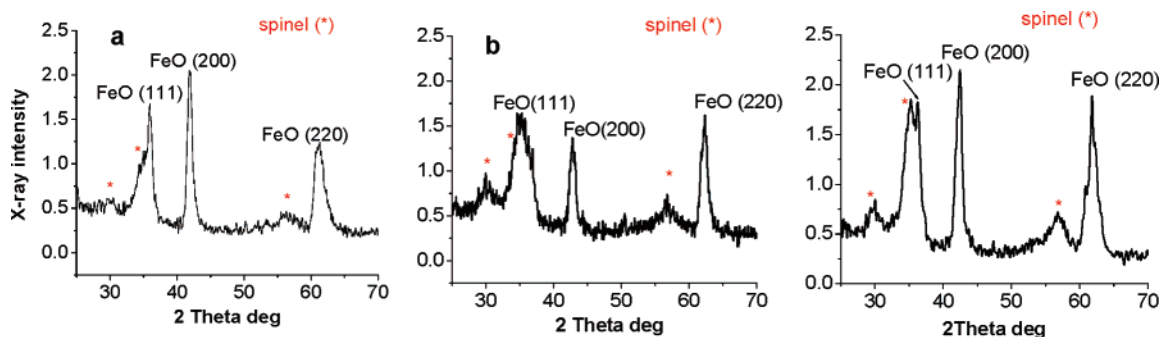


Figure 7. XRD profiles of (a) 20.1 and (b) 8.5 nm spherical and (c) 18.6 nm cubic iron oxide NPs.

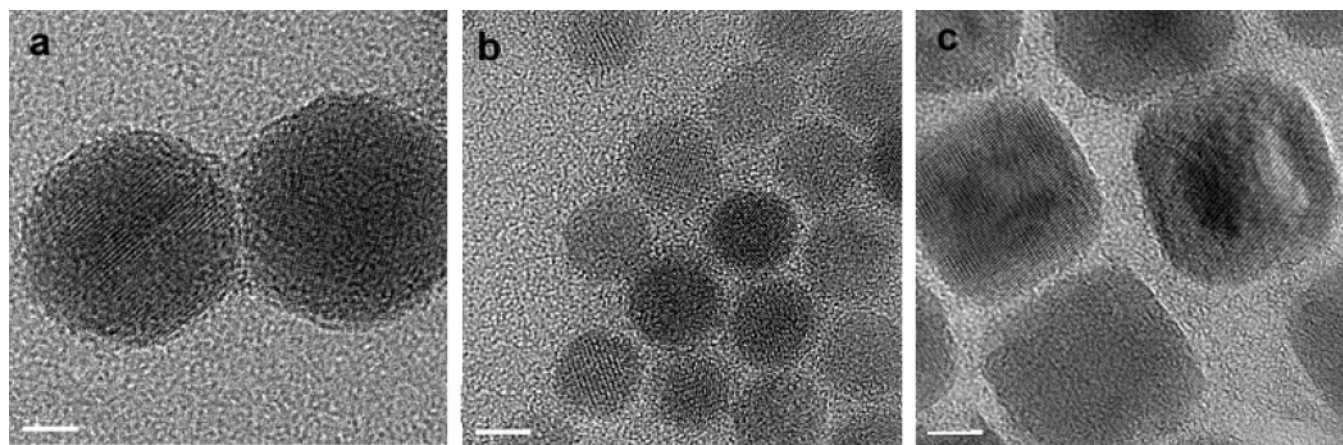


Figure 8. HRTEM images of the (a) 20.1, (b) 8.5, and (c) 18.6 nm (cube) NPs. The scale bar is 5 nm.

discussed above, the nucleation for FeOI-4, occurs at a higher temperature (Figure 3) than for FeOI-2, and therefore, it results in a larger amount of nuclei and consequently smaller nanoparticle sizes. It is noteworthy that in similar conditions, decomposition of FeOI-3 yields polydisperse nanoparticles (Figure 6b): the spherical particles measure between 14 and 28 nm. Moreover, in Figure 6b, one can see the particle fusion (red arrows) leading to the formation of short rods (green arrows). We believe that due to small separation of nucleation and growth processes (only 5 °C on the DSC trace) when FeOI-3 is used as a precursor, the synthesis of monodisperse NPs is difficult. It is noteworthy that all four precursors require different reaction temperatures to form monodisperse particles, so different saturated hydrocarbons were selected as the solvents of choice.

3.2.2. XRD and HRTEM. The XRD profiles of 20.1 and 8.5 nm nanoparticles presented in panels a and b of Figure 7 cannot be attributed to single crystals but rather to the presence of two phases: ferrous oxide wüstite (Fe_{1-x}O)¹⁵ (where x can be between 0.05 and 0.17) and a spinel phase that could correspond to either maghemite ($\gamma\text{-Fe}_2\text{O}_3$) or magnetite (Fe_3O_4).³² Because of line broadening of NPs, magnetite and maghemite cannot be distinguished in the XRD spectra. Wüstite is normally formed in the situation of an insufficient amount of oxidizing species or oxygen.^{13,32} For example, Casula et al.³² found that only multiple injections of oxidizer allowed the formation of maghemite, whereas a single injection led to the polymorph containing wüstite. Because wüstite is a metastable phase, under certain

conditions, it can be transformed into a mixture of wüstite, $\alpha\text{-Fe}$, and magnetite,¹³ yet $\alpha\text{-Fe}$ tends to accumulate in the particle shell, where it is easily oxidized when the sample is exposed to air and can go undetected. The XRD profiles presented in Figure 7 do not contain reflections characteristic of $\alpha\text{-Fe}$. Much more intense and narrow signals of the ferrous oxide (especially for larger particles) are consistent with the larger (Fe_{1-x}O) nanocrystals. Because wüstite and magnetite are very compatible both structurally and compositionally,^{32,33} the presence of both domains in a nanoparticle is reasonable. Formation of magnetite seeds between (Fe_{1-x}O) crystals in nanoparticles was reported earlier.¹³ A close look at the HRTEM images of 20.1 and 8.5 nm NPs (images a and b in Figure 8) shows that the central part of the particle is a single crystal, whereas the particle edge looks poorly organized. We believe that the more oxidized spinel is located in the particle shell. It is noteworthy that the higher XRD intensity signals of the spinel species is observed in the smaller particles with a larger surface-to-volume ratio.

The XRD profile of the cubic nanoparticles (Figure 7c) contains signals that can be assigned to both wüstite and spinel, yet the fraction of spinel is the largest among the particles synthesized. The HRTEM image of cubic particles (Figure 8c) also shows that they contain different crystalline domains in the interior and exterior of the nanoparticle. As was discussed earlier,¹³ if the reaction temperatures are sufficiently low not to favor decomposition of ferrous oxide into iron and magnetite, whereas the solvent and surfactant stabilize the particles, the spherical nuclei transform into

(32) Casula, M. F.; Jun, Y.-W.; Zaziski, D. J.; Chan, E. M.; Corrias, A.; Alivisatos, A. P. *J. Am. Chem. Soc.* **2006**, *128*, 1675.

(33) Ketteler, G.; Weiss, W.; Ranke, W.; Schlogl, R. *Phys. Chem. Chem. Phys.* **2001**, *3*, 1114.

cubes with {100} surfaces corresponding to the preferred shape of the rock salt structured wüstite. In our case, the cubic particles are not purely wüstite and we observe mainly spherical particles at lower temperatures (in octadecane), whereas the solvent stabilization properties are similar (octadecane and eicosane) and the Fe oleate precursor is the same; therefore, we think the process of favoring a certain shape of iron oxide nanoparticles (derived from iron oleate) is dependent on other factors. We believe the thermal behavior of the Fe oleate complex, i.e., the separation between nucleation and growth properties, along with the reaction temperature determine the size and shape of nanoparticles, but at present, no conclusions on the mechanism of cubic particle formation can be drawn.

Conclusions

We demonstrated the influence of the Fe oleate complex structure on its thermal properties and decomposition products, i.e., iron oxide nanoparticles, their size, size distribution, and structure. This study revealed that postsynthesis treatment (drying or extraction) affects the Fe oleate structure and thermal properties. The positions of endothermic transitions in the DSC traces of iron oleates, which can be assigned to nucleation and growth of nanoparticles, determine both the nanoparticle size and size distribution: the larger the separation between the nucleation and growth processes, the higher the probability of the monodisperse nanoparticle formation. We believe that the temperature separation

obtained from DSC traces has predictive power for any nanoparticle formation on the basis of thermal decomposition of a single precursor.

The nanoparticle size, size distribution, shape, and structure can be varied by controlling the reaction conditions (concentration, reaction temperature, and time) and the Fe oleate structure. Spherical monodisperse nanoparticles in the range 8.5–23.4 nm are obtained when the separation between nucleation and growth processes is at least ~ 10 °C. The XRD data show that iron oxide nanoparticles contain both wüstite ($\text{Fe}_{(1-x)}\text{O}$) and spinel (most likely Fe_3O_4), yet the fraction of spinel depends on the conditions of the nanoparticle formation. The largest spinel fraction was observed for 18 nm cubic nanoparticles.

Acknowledgment. This work has been supported, in part, by the NATO Science for Peace Program (Grant SFP-981438), NSF Grant BES-0322767, the IU FRSP and MetaCyt funds. The authors thank Bill Powell (JEOL) and Dr. Masahiro Kawasaki (JEOL) for the help with arranging and carrying out the HRTEM measurements at Michigan State University. The authors also thank Alexei Bykov (Tver Technical University, Russia) for XPS measurements.

Supporting Information Available: XPS, TEM, and XRD data. This material is available free of charge via the Internet at <http://pubs.acs.org>.

CM062948J